

# The role of Coulomb interaction in the superconducting properties of $\text{CaC}_6$ and H under pressure

S Massidda<sup>1</sup>, F Bernardini<sup>1</sup>, C Bersier<sup>2</sup>, A Continenza<sup>3</sup>,  
P Cudazzo<sup>3</sup>, A Floris<sup>2</sup>, H Glawe<sup>2</sup>, M Monni<sup>1</sup>, S Pittalis<sup>2</sup>, G Profeta<sup>3</sup>,  
A Sanna<sup>1</sup>, S Sharma<sup>2</sup> and E K U Gross<sup>2</sup>

<sup>1</sup> SLACS-INFN/CNR, and Dipartimento di Scienze Fisiche, Università degli Studi di Cagliari, I-09042 Monserrato (CA), Italy

<sup>2</sup> Institut für Theoretische Physik, Freie Universität Berlin, Arnimallee 14, D-14195 Berlin, Germany

<sup>3</sup> CNISM—Dipartimento di Fisica, Università degli Studi dell'Aquila, Via Vetoio 10, I-67010 Coppito (L'Aquila), Italy

Received 19 September 2008, in final form 10 December 2008

Published 28 January 2009

Online at [stacks.iop.org/SUST/22/034006](http://stacks.iop.org/SUST/22/034006)

## Abstract

Superconductivity in intercalated graphite  $\text{CaC}_6$  and H under extreme pressure is discussed in the framework of superconducting density functional theory. A detailed analysis of how the electron–phonon and electron–electron interactions combine together to determine the superconducting gap and critical temperature ( $T_c$ ) of these systems is presented. In particular, we discuss the effect on the calculated  $T_c$  of the anisotropy of the electron–phonon interaction and of the different approximations for screening the Coulomb repulsion. These results contribute to the understanding of multigap and anisotropic superconductivity, which has received a lot of attention since the discovery of  $\text{MgB}_2$ , and show how it is possible to describe the superconducting properties of real materials on a fully *ab initio* basis.

(Some figures in this article are in colour only in the electronic version)

## 1. Introduction

The discovery of two-gap superconductivity in  $\text{MgB}_2$  has triggered a huge revival of interest in the search for new electron–phonon superconductors. Recent experience in the vast majority of electron–phonon superconductors has shown that *ab initio* calculations can provide a detailed and useful description of the normal state of these systems, including dynamical properties and electron–phonon (e–ph) coupling. The treatment of the superconducting state, however, is a much more difficult task. On the theoretical side, most calculations nowadays are based on the Eliashberg theory [1–3]. While in the Eliashberg theory the electron–phonon interaction is perfectly accounted for, the effects of the electron–electron (e–e) Coulomb repulsion are condensed in a single parameter,  $\mu^*$ , which is difficult to calculate from first principles and which, in most practical applications, is treated as an adjustable parameter usually fitted to the experimental critical temperature,  $T_c$ . In this sense, the Eliashberg theory, in spite

of its tremendous success, has to be considered as a semi-phenomenological theory. However, the possibility to describe the superconducting state on a fully *ab initio* ground and, as a consequence, to be able to predict the superconducting properties of materials, is still highly sought after.

Density functional theory (DFT), a very successful standard approach in normal state electronic structure calculations, has recently been extended to deal with the superconducting (SC) state (SCDFT) [4, 5]. SCDFT contains no adjustable parameters, and the final critical temperature is the result of material-specific quantities, all of them computed *ab initio*. SCDFT is able to treat superconductors with a wide range of couplings, as shown by several investigations,  $\text{MgB}_2$  being one of the most nontrivial one [6].

Superconductivity is the result of a subtle competition between two opposite effects: the phonon-mediated attraction (e–ph in the following) and the direct Coulomb repulsion (e–e) between the electrons. In this work, we show how different approximations for the e–e and e–ph interactions

(e.g. an isotropic approximation, or an insufficiently elaborated screening entering the e–e term) will depart from the experimental results. Considering intercalated graphite  $\text{CaC}_6$  and H under pressure as test cases, we will quantify, without ad hoc assumptions, the effect on  $T_c$  of the superconducting gap anisotropy and of the assumed screened Coulomb potential. The choice of these two systems comes from their peculiarities.  $\text{CaC}_6$  is a superconductor with a moderate degree of anisotropy [7], recently confirmed by experiments [8, 9], with electronic bands having different orbital characters. With a critical temperature as high as 11.5 K,  $\text{CaC}_6$  exhibits the highest  $T_c$  [10] among graphite intercalated compounds. DFT calculations of the electronic and dynamical properties of  $\text{CaC}_6$  [11, 12] pointed out that the e–ph coupling is large enough to yield the observed  $T_c$ . In  $\text{CaC}_6$ , the phonons mostly contributing to superconductivity belong to an optical branch involving Ca displacements and, to a lower extent, to two C-related branches at much higher frequency. The different phonon branches couple to different Fermi surface (FS) sheets, as pointed out in [7].

High temperature superconductivity in H was suggested 40 years ago by Ashcroft [13], and has been the subject of several investigations (see [14] and references therein), both theoretical and experimental. However, metalization of hydrogen is far than being obvious and easy to reach. Experimentally, in the search for metallic hydrogen, only three different insulating phases were found at pressures as large as 350 GPa [15]. Unlike  $\text{CaC}_6$ , molecular hydrogen under pressure involves basically only one type of atomic orbital; it has very large phonon frequencies (due to the light H mass) and large e–ph coupling [14].

The paper is organized as follows. In section 2 we summarize the main features of SCDFT and describe our computational approach; in section 3 we discuss the different approximations used for the Coulomb interaction; in sections 4 and 5 we present our results for  $\text{CaC}_6$  and H, respectively; finally, in section 6, we summarize our conclusions.

## 2. Density functional theory for superconductors

Density functional theory [17] has enjoyed increasing popularity as a reliable and relatively inexpensive tool to describe real materials. In this section we will briefly outline the DFT approach to superconductivity, and refer to the original papers for more details. In order to give an introduction to SCDFT, it is instructive to recall how magnetism is treated within DFT. The Hohenberg–Kohn (HK) theorem [18] states that all observables, in particular the magnetization, are functionals of the electronic density *alone*. This, however, assumes the knowledge of the magnetization as a functional of the density. Finding an approximation for this functional is extremely hard and, in practice, one chooses a different approach. The task can be vastly simplified by treating the magnetization density  $\mathbf{m}(\mathbf{r})$ , i.e., the order parameter of the magnetic state, as an additional fundamental density in the density functional framework [19]. An auxiliary field—here a magnetic field  $\mathbf{B}_{\text{ext}}(\mathbf{r})$ —is introduced, which couples to  $\mathbf{m}(\mathbf{r})$  and breaks the corresponding (rotational)

symmetry of the Hamiltonian. This field drives the system into the ordered state. If the system is actually magnetic, the order parameter will survive when the auxiliary perturbation is quenched. In this way, the ground-state magnetization density is determined by minimizing the total energy functional (free energy functional for finite temperature calculations) with respect to both the normal density and the magnetization density. Within this approach, much simpler approximations to the exchange–correlation (xc) functional (now a functional of two densities) can lead to satisfactory results.

The same idea is also at the heart of density functional theory for superconductors, as formulated by Oliveira, Gross and Kohn (OGK) [16]. Here the order parameter is the so-called anomalous density,

$$\chi(\mathbf{r}, \mathbf{r}') = \langle \hat{\Psi}_{\uparrow}(\mathbf{r}) \hat{\Psi}_{\downarrow}(\mathbf{r}') \rangle, \quad (1)$$

and the corresponding potential is the non-local pairing potential  $\Delta(\mathbf{r}, \mathbf{r}')$ . It can be interpreted as an external pairing field, induced by an adjacent superconductor via the proximity effect. Again, this external field only acts to break the symmetry (here the gauge symmetry) of the system, and is quenched at the end of the calculation. As in the case of magnetism, if the system is actually a superconductor the order parameter will be sustained by the self-consistent effective pairing field. The approach outlined so far captures, in principle, all the electronic degrees of freedom. To describe conventional phonon-mediated superconductors, the electron–phonon interaction also has to be taken into account.

In order to treat both weak and strong electron–phonon coupling, the electronic and the nuclear degrees of freedom have to be treated on an equal footing. This can be achieved by a multi-component DFT, based on both the electronic density and the nuclear density [20, 21]. In addition to the normal and anomalous electronic densities, we also include the diagonal of the nuclear density matrix

$$\Gamma(\mathbf{R}) = \langle \hat{\Phi}^{\dagger}(\mathbf{R}_1) \dots \hat{\Phi}^{\dagger}(\mathbf{R}_N) \hat{\Phi}(\mathbf{R}_N) \dots \hat{\Phi}(\mathbf{R}_1) \rangle, \quad (2)$$

where  $\hat{\Phi}(\mathbf{R})$  is a nuclear field operator<sup>4</sup>.

In order to formulate a Hohenberg–Kohn theorem for this system, we introduce a set of three potentials, which couple to the three densities described above. Since the electron–nuclear interaction, which in conventional DFT constitutes the external potential, is treated explicitly in this formalism, it is *not* part of the external potential. The nuclear Coulomb interaction  $\hat{U}^{\text{nn}}$  already has the form of an external many-body potential, coupling to  $\Gamma(\mathbf{R})$ , and for the sake of the Hohenberg–Kohn theorem, this potential will be allowed to take the form of an arbitrary  $N$ -body potential. All three external potentials are merely mathematical devices, required to formulate a Hohenberg–Kohn theorem. At the end of the derivation, the external electronic and pairing potentials will be set to zero while the external nuclear many-body potential to the nuclear Coulomb interaction.

<sup>4</sup> We note that taking only the nuclear density would lead to a system of strictly non-interacting nuclei which would give rise to non-dispersive, hence unrealistic, phonons.

As usual, the Hohenberg–Kohn theorem guarantees a one-to-one mapping between the set of the densities  $\{n(\mathbf{r}), \chi(\mathbf{r}, \mathbf{r}'), \Gamma(\mathbf{R})\}$  in thermal equilibrium and the set of their conjugate potentials  $\{v_{\text{ext}}^e(\mathbf{r}) - \mu, \Delta_{\text{ext}}(\mathbf{r}, \mathbf{r}'), v_{\text{ext}}^n(\mathbf{R})\}$ . Therefore, all the observables are functionals of the set of densities. Finally, it assures that the grand canonical potential,

$$\begin{aligned} \Omega[n, \chi, \Gamma] = & F[n, \chi, \Gamma] + \int d^3r n(\mathbf{r})[v_{\text{ext}}^e(\mathbf{r}) - \mu] \\ & - \int d^3r \int d^3r' [\chi(\mathbf{r}, \mathbf{r}')\Delta_{\text{ext}}^*(\mathbf{r}, \mathbf{r}') + \text{h.c.}] \\ & + \int d^3R \Gamma(\mathbf{R})v_{\text{ext}}^n(\mathbf{R}), \end{aligned} \quad (3)$$

is minimized by the equilibrium densities. We use the notation  $A[f]$  to denote that  $A$  is a functional of  $f$ . The functional  $F[n, \chi, \Gamma]$  is universal, in the sense that it does not depend on the external potentials, and is defined by

$$\begin{aligned} F[n, \chi, \Gamma] = & T^e[n, \chi, \Gamma] + T^n[n, \chi, \Gamma] + U^{\text{en}}[n, \chi, \Gamma] \\ & + U^{\text{ee}}[n, \chi, \Gamma] - \frac{1}{\beta} S[n, \chi, \Gamma], \end{aligned} \quad (4)$$

where  $S$  is the entropy of the system,

$$S[n, \chi, \Gamma] = -\text{Tr}\{\hat{\rho}_0[n, \chi, \Gamma] \ln(\hat{\rho}_0[n, \chi, \Gamma])\}. \quad (5)$$

In standard DFT one normally defines a Kohn–Sham system, i.e., a non-interacting system chosen such that it has the same ground-state density as the interacting one. The variational procedure for this system gives Schrödinger-like (Kohn–Sham) equations for non-interacting electrons subject to an effective (Kohn–Sham) potential. These equations are nowadays routinely solved by solid state theorists. In our formalism, the Kohn–Sham system consists of non-interacting (superconducting) electrons, and *interacting* nuclei. We will not describe here the details of the method, and will only outline its basic features: the Kohn–Sham potentials, which are derived in analogy to normal DFT, include the external fields, Hartree, and exchange–correlation terms. The latter account for all many-body effects of the electron–electron and electron–nuclear interactions. Obtaining their explicit form has represented a major theoretical effort [22–24]. Once this problem has been solved, the problem of minimizing the Kohn–Sham grand canonical potential can be transformed into a set of three differential equations that have to be solved self-consistently: one equation for the nuclei, which resembles the familiar nuclear Born–Oppenheimer equation, and two coupled equations which describe the electronic degrees of freedom and have the algebraic structure of the Bogoliubov–de Gennes [25] equations.

The resulting Kohn–Sham–Bogoliubov–de Gennes (KS–BdG) equations read (we use atomic Rydberg units)

$$\begin{aligned} \left[ -\frac{\nabla^2}{2} + v_s^e(\mathbf{r}) - \mu \right] u_{n\mathbf{k}}(\mathbf{r}) + \int d^3r' \Delta_s(\mathbf{r}, \mathbf{r}') v_{n\mathbf{k}}(\mathbf{r}') \\ = \tilde{E}_{n\mathbf{k}} u_{n\mathbf{k}}(\mathbf{r}), \end{aligned} \quad (6a)$$

$$\begin{aligned} -\left[ -\frac{\nabla^2}{2} + v_s^e(\mathbf{r}) - \mu \right] v_{n\mathbf{k}}(\mathbf{r}) + \int d^3r' \Delta_s^*(\mathbf{r}, \mathbf{r}') u_{n\mathbf{k}}(\mathbf{r}') \\ = \tilde{E}_{n\mathbf{k}} v_{n\mathbf{k}}(\mathbf{r}), \end{aligned} \quad (6b)$$

where  $u_{n\mathbf{k}}(\mathbf{r})$  and  $v_{n\mathbf{k}}(\mathbf{r})$  are the particle and hole amplitudes. This equation is very similar to the Kohn–Sham equations in the OGK formalism [16]. However, in the present formulation the lattice potential is not considered an external potential but enters via the electron–ion Hartree term. Furthermore, our exchange–correlation potentials depend on the nuclear density matrix, and therefore on the phonons. Although equations (6) and the corresponding equations for the nuclei have the structure of static mean-field equations, they contain, in principle, all correlation and retardation effects through the exchange–correlation potentials.

These KS–BdG equations can be simplified by the so-called decoupling approximation [4, 26], which corresponds to the following ansatz for the particle and hole amplitudes:

$$u_{n\mathbf{k}}(\mathbf{r}) \approx u_{n\mathbf{k}} \varphi_{n\mathbf{k}}(\mathbf{r}); \quad v_{n\mathbf{k}}(\mathbf{r}) \approx v_{n\mathbf{k}} \varphi_{n\mathbf{k}}(\mathbf{r}), \quad (7)$$

where the wavefunctions  $\varphi_{n\mathbf{k}}(\mathbf{r})$  are the solutions of the normal Schrödinger equation. In this way the eigenvalues in equations (6) become  $\tilde{E}_{n\mathbf{k}} = \pm E_{n\mathbf{k}}$ , where

$$E_{n\mathbf{k}} = \sqrt{\xi_{n\mathbf{k}}^2 + |\Delta_{n\mathbf{k}}|^2}, \quad (8)$$

and  $\xi_{n\mathbf{k}} = \epsilon_{n\mathbf{k}} - \mu$ . This form of the eigenenergies allows us to interpret the pair potential  $\Delta_{n\mathbf{k}}$  as the gap function of the superconductor. Furthermore, the coefficients  $u_{n\mathbf{k}}$  and  $v_{n\mathbf{k}}$  are given by simple expressions within this approximation:

$$u_{n\mathbf{k}} = \frac{1}{\sqrt{2}} \text{sgn}(\tilde{E}_{n\mathbf{k}}) e^{i\phi_{n\mathbf{k}}} \sqrt{1 + \frac{\xi_{n\mathbf{k}}}{\tilde{E}_{n\mathbf{k}}}}, \quad (9a)$$

$$v_{n\mathbf{k}} = \frac{1}{\sqrt{2}} \sqrt{1 - \frac{\xi_{n\mathbf{k}}}{\tilde{E}_{n\mathbf{k}}}}. \quad (9b)$$

Finally, the matrix elements  $\Delta_{n\mathbf{k}}$  are defined as

$$\Delta_{n\mathbf{k}} = \int d^3r \int d^3r' \varphi_{n\mathbf{k}}^*(\mathbf{r}) \Delta_s(\mathbf{r}, \mathbf{r}') \varphi_{n\mathbf{k}}(\mathbf{r}'), \quad (10)$$

and  $\phi_{n\mathbf{k}}$  is the phase  $e^{i\phi_{n\mathbf{k}}} = \Delta_{n\mathbf{k}}/|\Delta_{n\mathbf{k}}|$ . The normal and the anomalous densities can then be easily obtained from

$$n(\mathbf{r}) = \sum_{n\mathbf{k}} \left[ 1 - \frac{\xi_{n\mathbf{k}}}{E_{n\mathbf{k}}} \tanh\left(\frac{\beta}{2} E_{n\mathbf{k}}\right) \right] |\varphi_{n\mathbf{k}}(\mathbf{r})|^2 \quad (11a)$$

$$\chi(\mathbf{r}, \mathbf{r}') = \frac{1}{2} \sum_{n\mathbf{k}} \frac{\Delta_{n\mathbf{k}}}{E_{n\mathbf{k}}} \tanh\left(\frac{\beta}{2} E_{n\mathbf{k}}\right) \varphi_{n\mathbf{k}}(\mathbf{r}) \varphi_{n\mathbf{k}}^*(\mathbf{r}'). \quad (11b)$$

Within the decoupling approximation, we finally arrive at an equation for the  $\mathbf{k}$ -resolved superconducting gap  $\Delta_{n\mathbf{k}}$ , which has the following form [4, 5, 16, 27]:

$$\Delta_{n\mathbf{k}} = -\mathcal{Z}_{n\mathbf{k}} \Delta_{n\mathbf{k}} - \frac{1}{2} \sum_{n'\mathbf{k}'} \mathcal{K}_{n\mathbf{k}, n'\mathbf{k}'} \frac{\tanh\left(\frac{\beta}{2} E_{n'\mathbf{k}'}\right)}{E_{n'\mathbf{k}'}} \Delta_{n'\mathbf{k}'}. \quad (12)$$

Equation (12) is the central equation of the DFT for superconductors. The kernel  $\mathcal{K}$  consists of two contributions  $\mathcal{K} = \mathcal{K}^{\text{e-ph}} + \mathcal{K}^{\text{e-e}}$ , representing the effects of the e–ph and of the e–e interactions, respectively. The diagonal term  $\mathcal{Z}$  plays

a similar role as the renormalization term in the Eliashberg equations (no analogous renormalization is included, in the present status of the theory, for the normal channel). Explicit expressions of  $\mathcal{K}^{e-ph}$  and  $\mathcal{Z}$ , which are the results of the approximate functionals, are given in equations (9) and (11) of [5], respectively. These two terms involve the e-ph coupling matrix, while  $\mathcal{K}^{e-e}$  contains the matrix elements of the screened Coulomb interaction (the explicit expression is given below). Equation (12) has the same structure as the BCS gap equation, with the *ab initio* kernel  $\mathcal{K}$  replacing the model interaction of BCS theory (which allows for the predictive power absent within BCS theory). This similarity allows us to interpret the kernel as an effective interaction responsible for the binding of the Cooper pairs. Moreover, we emphasize that equation (12) is not a mean-field equation (as in BCS theory), since it contains correlation effects via the SC exchange–correlation functional entering  $\mathcal{K}$  and  $\mathcal{Z}$ . Furthermore, it has the form of a static equation—i.e., it does not depend *explicitly* on the frequency—and therefore has a simpler structure (and is computationally more manageable) than the Eliashberg equations. However, this certainly does not imply that retardation effects are absent from the theory. Once again, retardation effects enter through the xc functional, as explained in [4, 5]. Various tests [24] have shown that, in a model superconductor without Coulomb repulsion, SCDFT provides results very close to those obtained within Eliashberg theory. SCDFT, however, allows us to treat the e-ph and the screened e-e interactions on the same footing, which has never been done within Eliashberg theory. This is definitely a point of strength of our approach, relative to Eliashberg theory. On the other hand, due to the static character of our gap equation (we are not using a Green function approach), the full wavevector and frequency-dependent gap function are not accessible to our calculation. We, therefore, only obtain an energy dependence of the SC gap through its  $k$ -point dependence ( $\Delta(\xi_{\mathbf{k}}) = \Delta(n\mathbf{k})$ ). A frequency-dependent gap function may be retrieved from the dynamical response functions [28] associated with the time-dependent version [29] of SCDFT. This possibility, however, has not been exploited in practice so far.

The Coulomb interaction terms can be treated at different levels of approximation, as we will discuss below. It is important to point out, however, that common to all these methods is the need to consider a very large energy range (we used up to  $\approx 2$  Ryd). This is necessary to bring about the retardation effects associated to the different phononic and electronic timescales. It has been shown in figure 9 of [5] how the gap at  $E_F$  converges as a function of the energy cutoff in equation (12). The presence of a node in the energy dependence of the gap implies a constructive contribution to  $\Delta(n, \mathbf{k}_F)$  from the states away from  $E_F$ , through a repulsive interaction. It is a key feature of our approach that the matrix elements of the screened Coulomb interaction are used in the kernel of the gap equation up to very high energies. It is this feature that allows for the description of nontrivial, material-specific effects. Traditionally, the use of this large energy window is avoided by rescaling the Fermi surface average of these matrix elements. This rescaling leads to the Morel–Anderson pseudopotential  $\mu^*$ , which is absent in our approach.

In the most accurate implementation of our theory, we calculated the screened Coulomb matrix elements (MEs) with respect to the Bloch functions, for the whole energy range of relevant valence and conduction states. The different nature of the electronic bands in each material (e.g. some of them can be highly localized while others more delocalized), strongly calls for the use of a non-diagonal screening, including local field effects. In order to properly describe these effects, a very important step to achieve good agreement with the experiment, we calculated the static random phase approximation (RPA) dielectric matrix (DM)  $\epsilon^{-1}(\mathbf{q}, \mathbf{G}, \mathbf{G}')$ , using the pseudopotential-based SELF code [30]. The explicit expression of the kernel  $\mathcal{K}^{e-e}$  in reciprocal space reads

$$\mathcal{K}_{n\mathbf{k}, n'\mathbf{k}'}^{e-e} = 4\pi \sum_{\mathbf{G}, \mathbf{G}'} \epsilon^{-1}(\mathbf{q}, \mathbf{G}, \mathbf{G}') \times \frac{\langle n'\mathbf{k}' | e^{i(\mathbf{q}+\mathbf{G})\cdot\mathbf{r}} | n\mathbf{k} \rangle \langle n\mathbf{k} | e^{-i(\mathbf{q}+\mathbf{G}')\cdot\mathbf{r}} | n'\mathbf{k}' \rangle}{|\mathbf{q} + \mathbf{G}| |\mathbf{q} + \mathbf{G}'|}, \quad (13)$$

where  $\mathbf{q} = \mathbf{k}' - \mathbf{k}$ . The detailed structure, energy, and  $\mathbf{k}$ -dependence of the kernel  $\mathcal{K}^{e-e}$  change the Coulomb renormalization effect (due to the different scales of the vibrational and electronic energies) considered: in many materials, it only acts as a scaling of the superconducting gap at the Fermi energy, thus keeping the main structures of the coupling (see [7, 31–33]). On the other hand, in strongly anisotropic materials with small interband interaction (like MgB<sub>2</sub>), the Coulomb renormalization turns out to be nontrivial [6, 34].

In this paper we report a study of the role of the different approximations for the Coulomb and the electron–phonon interactions on the solution of the SCDFT gap equation. This is illustrated in CaC<sub>6</sub> [7] and H under extreme pressure. As mentioned above, the normal state calculations, necessary for the study of the superconducting state, are performed within DFT in the LDA or GGA approximations. Computationally, the electronic and dynamical properties are obtained using the pseudopotential method as implemented in the QUANTUM-ESPRESSO package [35]; the screened Coulomb matrix elements are obtained with the SELF [30] code.

### 3. Evaluation of Coulomb matrix elements

In this section we discuss the different approximate formulations of the Coulomb interaction analyzed in this work.

#### 3.1. Sham–Kohn

The first and simplest approximation includes a Thomas–Fermi (TF) dielectric function together with free-electron wavefunctions. This leads to isotropic (i.e.  $\mathbf{k}$  independent) matrix elements, expressed by the analytic formula [4, 5]:

$$K_{\xi, \xi'}^{e-e} = \frac{\pi}{2\sqrt{\xi\xi'}} \ln \left[ \frac{\xi + \xi' + 2\sqrt{\xi\xi'} + q_{TF}^2/2}{\xi + \xi' - 2\sqrt{\xi\xi'} + q_{TF}^2/2} \right], \quad (14)$$

where the Fermi level is fixed by the number of valence electrons and the TF wavevector is that of a jellium having the same density of states at the Fermi energy of the true system  $N(0)$ , i.e.  $q_{TF}^2 = 8\pi N(0)$ . A justification for



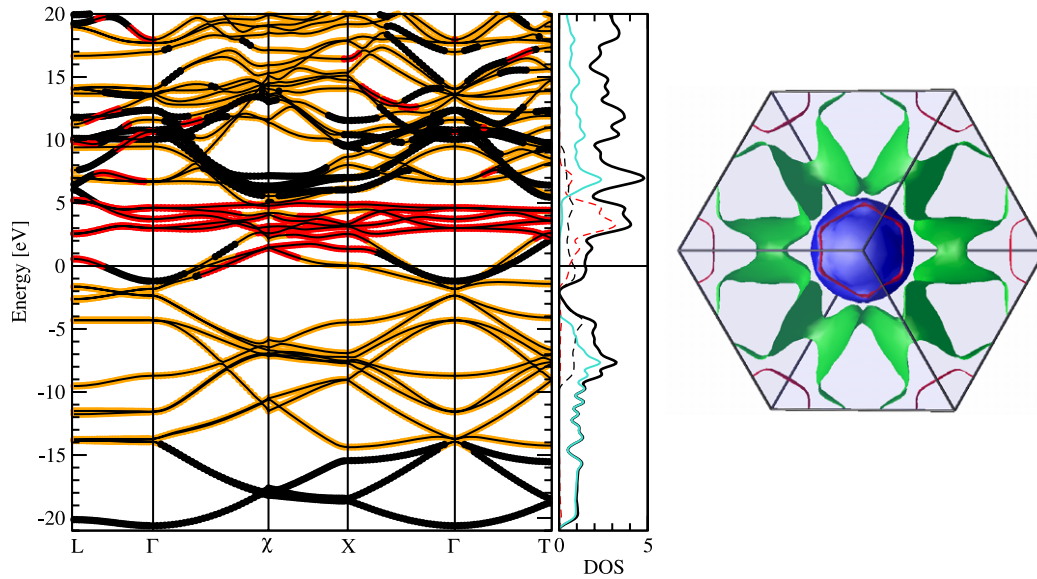


**Figure 1.** Left panel: electronic band structure of  $\text{CaC}_6$ , with the Fermi energy set to zero. Different colors for the Kohn–Sham eigenvalues are used corresponding to the s (black) p (orange—light gray) or d (red—gray) main orbital character. Central panel: total density of states (DOS) (thick black line), projected DOS on Ca site (dashed red—gray line) and on C states, divided in  $\text{sp}^2$  part (turquoise—light gray), and  $\text{p}_z$  part (long dashed black). Right panel:  $\text{CaC}_6$  Fermi surface, showing the external  $\pi$  sheet (1, green (light gray)), the Ca-related sphere (2, blue (dark gray)) and the internal  $\pi$  sheet (3, red (hexagonal shapes)).

the use of this approximation, in the spirit of the seminal paper of Sham and Kohn [39], is given in [4]. Typically, equation (14) provides reasonable results for systems with delocalized electrons [5, 32]. Furthermore, it avoids the cumbersome calculation of the anisotropic Coulomb matrix elements, calculated with the Kohn–Sham Bloch functions of the system (see below).

### 3.2. Bloch wavefunctions and Thomas–Fermi screening

In order to include the effects of the wavefunction localization in the evaluation of the matrix elements, we used the real Kohn–Sham Bloch states of equation (13), together with the TF screened dielectric function. The TF vector is again  $q_{\text{TF}}^2 = 8\pi N(0)$ , where  $N(0)$  is the density of states at the Fermi energy in the real material. In this way, we correct for the locality of the wavefunctions in the evaluation of the Coulomb integrals, still keeping, for the screening, a very approximate form. The present approximation and those described below in this section correspond to an anisotropic treatment of the Coulomb interaction.

### 3.3. Diagonal random phase approximation (RPA)

The TF dielectric function is only valid in the limit  $\mathbf{q} \rightarrow 0$ . To improve this aspect we calculate the dielectric function  $\epsilon(\mathbf{q}, \mathbf{G}, \mathbf{G}')$  in the RPA, initially limiting ourselves to the diagonal form, where we set to zero all the  $\mathbf{G} \neq \mathbf{G}'$  terms. In real space this corresponds to a screening depending not on  $\mathbf{r}$  and  $\mathbf{r}'$  separately but only on  $\mathbf{r} - \mathbf{r}'$ . On the other hand, the electronic polarizability is built by taking into account the real band structure of the system. This approximation is expected to be reasonable for closely packed systems with delocalized electrons.

### 3.4. Non-diagonal RPA

With a fully non-local RPA screening (with non-zero  $\mathbf{G} \neq \mathbf{G}'$  terms) the electronic response will depend on the two spatial indices  $\mathbf{r}$  and  $\mathbf{r}'$  separately. This improves the efficiency of the screening for strongly localized states, with a resulting reduction of the Coulomb matrix elements in the corresponding regions. As an example, this improvement affects mainly the graphene sheets in  $\text{CaC}_6$ .

## 4. Results on $\text{CaC}_6$

Before discussing the various approximations for the Coulomb interaction, we briefly describe the electronic states of  $\text{CaC}_6$ . This material crystallizes in the rhombohedral space group  $R\bar{3}m$  [10], and has one unit formula per primitive cell. The rhombohedral lattice parameter is 5.17 Å, with rhombohedral angle 49.55°. We plot in figure 1 the band structure of the system. Three bands cross the Fermi energy. Two of them have p character and come from the  $\pi$  bonding pattern of the graphene layer. They give rise to two two-dimensional Fermi surfaces (figure 1, right panel). The third band corresponds to a spherical Fermi surface with the charge localized in the interlayer space and on the Ca ion. Its character is mainly s (d) in the  $k_x, k_y$  ( $k_z$ ) directions (the z-axis being normal to the graphene layer).

The presence of an intercalant band crossing the Fermi energy has been shown to be a necessary condition for superconductivity in graphite intercalated compounds (GICs), as pointed out by Csányi *et al* [36]. Interlayer bands, uncorrelated to a particular atomic orbital nature, have been largely discussed in graphite [40], GICs [11, 36–38] and  $\text{MgB}_2$  [6]. In  $\text{CaC}_6$ , however, this band gains a further strong

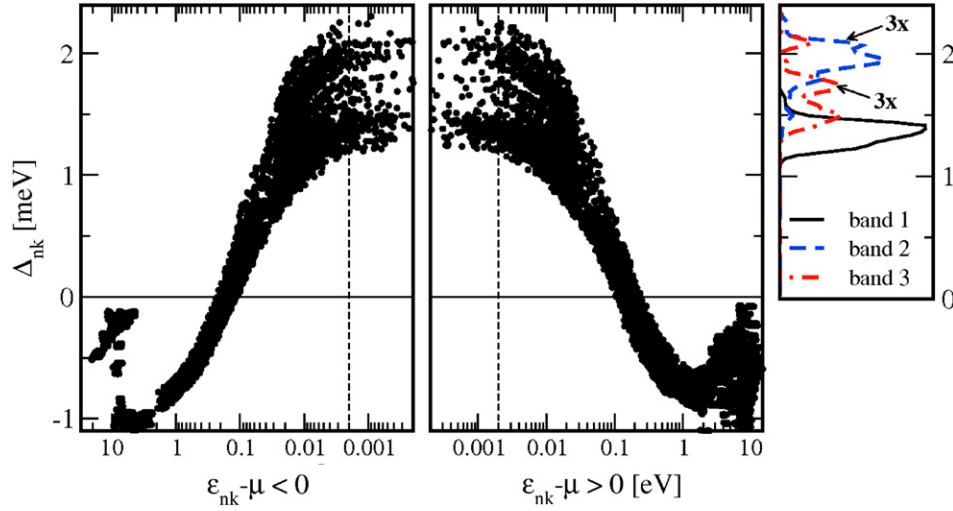


**Figure 2.**  $\text{CaC}_6$  superconducting gap  $\Delta_{nk}$  as a function of the energy distance from the Fermi energy ( $\mu$  in the figure). The right panel shows the energy distribution (in arbitrary units) of the gap, resolved over the three Fermi surfaces. The histogram is evaluated within the energy window from  $-2$  to  $2$  meV.

contribution from the Ca 4s and 3d orbitals. This band is coupled to the in-plane Ca optical phonon branch; these low frequency modes provide a strong contribution to the e-ph constant  $\lambda$  [7, 11, 12]. The energy window between  $-20$  and  $-4$  eV is mainly occupied by the bands forming the  $\text{sp}^2$  bonds pattern of graphene, as shown by the orbital decomposed density of states in figure 1. The  $p_z$  bands starts around the L symmetry point (corresponding to the A point in the hexagonal unit cell, i.e. to the zone boundary in  $z$  direction) at about  $-10$  eV. Just above the Fermi level, mainly between 2 and 5 eV, the DOS shows a peak originated by a set of flat bands due to Ca -d states. Above 5 eV the percentage of the total charge projected over atomic orbitals starts to reduce corresponding to the free-electron limit of the KS wavefunctions.

#### 4.1. Anisotropic approach for the Coulomb interaction

We now discuss the effect of the approximate treatments of the Coulomb interaction described in section 3 on the superconducting  $T_c$ . In the following analysis, we assume a fully anisotropic phononic kernel. Within the Sham–Kohn approximation we obtain  $T_c = 13.5$  K, to be compared with the experimental value  $T_c^{\text{exp}} = 11.5$  K. The Sham–Kohn approximation is rather simple and gives quite reliable results for nearly free-electron metals [5, 32]. However, for  $\text{CaC}_6$  this approximation is not expected to hold, since it neglects the presence of localized states with much stronger Coulomb interactions. Therefore in the Sham–Kohn approximation an overestimate of the superconducting gap and  $T_c$  is expected and found.

With the Thomas–Fermi approximation and Bloch wavefunctions we obtain  $T_c \approx 8.2$  K, underestimating the experimental value. Remarkably, the critical temperature obtained using the RPA approximation with diagonal screening turns out to be  $T_c \approx 8.0$  K, very close to the one found in the TF approach and significantly smaller than the experimental value. This result shows that the TF screening is quite

**Table 1.** Band-resolved superconducting gap of  $\text{CaC}_6$  from different approximation schemes for the e–e interaction. The brackets  $\langle \dots \rangle$  indicate a Fermi surface average and the indices 1, 2, 3 correspond to the three parts of the Fermi surface (see figure 1), namely the external (green (light gray))  $\pi$  surface, the Ca sphere (blue (dark gray)) and the internal (red (hexagonal shapes))  $\pi$  surface.

	SK-TF	wf-TF	diag-RPA	RPA	No Coulomb
$\langle \Delta_1 \rangle$ (meV)	2.20	1.24	1.19	1.42	5.40
$\langle \Delta_2 \rangle$ (meV)	2.94	1.78	1.77	2.00	6.72
$\langle \Delta_3 \rangle$ (meV)	2.49	1.39	1.37	1.67	6.08
$T_c$ (K)	13.5	8.2	8.0	9.4	31

similar to the static diagonal RPA one, and that indeed the  $T_c$  underestimation is related to the lack of local field corrections. A diagonal screening in fact averages out over a unit cell of the system. A correct screening, on the other hand, should be more effective in regions of the unit cell with larger charge density. As a consequence, inclusion of non-diagonal terms in the screening produces an increased  $T_c$  of 9.4 K. This value, while not in excellent agreement with the experiment, represents an improvement over the previous  $T_c$  values (we recall that in our calculations no fitting parameter to the experiment is used). In table 1 we summarize the superconducting properties in the discussed cases, including  $T_c$  and the value of the gap  $\Delta_{nk}$  on the different Fermi surface sheets.

The detailed behavior of the gap  $\Delta_{nk}$  as a function of the normal state eigenvalue is given in figure 2. The set of black points shows the gap at  $T = 0$  K, as a function of the energy distance from the Fermi level  $E_F$ . For each energy the gap is not a single-valued function, i.e. the gap is anisotropic in the reciprocal space. In particular, the gap values exhibit a moderate anisotropy, rather than a multigap character.

#### 4.2. Isotropic approach for the Coulomb interaction

All the above results (excluding the Sham–Kohn approximation) refer to fully anisotropic calculations, in which the  $\mathbf{k}$ ,  $\mathbf{k}'$

**Table 2.** Results of the RBCS equation including both the e-ph ( $\lambda_{ij}$ ) and e-e ( $\mu_{ij}$ ) matrices (Full RBCS), and without the  $\mu_{ij}$  matrix (RBCS (e-ph)).

	$\Delta_1/\Delta_3$	$\Delta_2/\Delta_3$
Full RBCS	1.61	1.13
RBCS (e-ph)	1.37	1.09

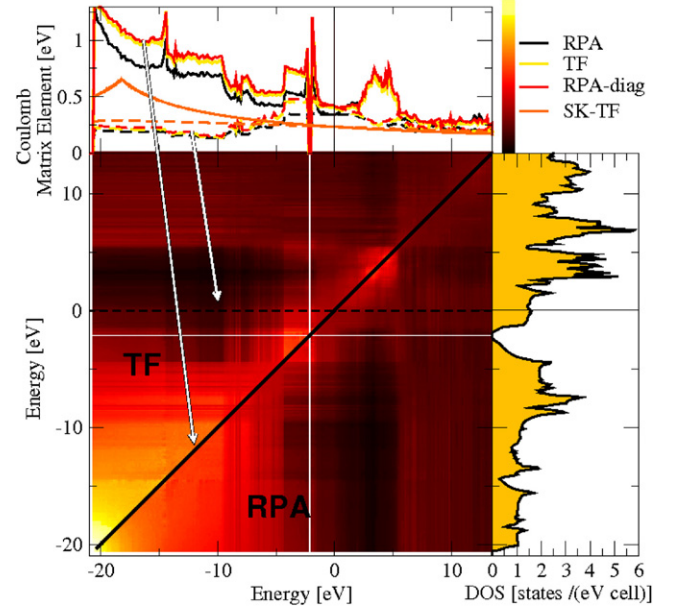
dependence of the Coulomb matrix elements is included in the solution of the SCDFT gap equation. We also calculated  $T_c$  with an isotropic approach in which the  $K_{n\mathbf{k},n'\mathbf{k}'}$  matrix elements are averaged in  $\mathbf{k}$  and  $\mathbf{k}'$  over isoenergy surfaces, yielding a corresponding  $V(\xi, \xi')$  function. The average is done for each one of the approximations discussed. The critical temperatures turn out to be quite close (within the order of few per cent) to the corresponding fully anisotropic ones, showing that the anisotropy effect on the Coulomb repulsion is almost negligible, unlike in the case of  $\text{MgB}_2$  [6, 34]. On the other hand (see section 4.3), this is not true for the phononic part of the kernel [7–9].

A graphical comparison between the (averaged) different approximations is given in figure 3, where we report (upper panel) two cuts of the function  $V(\xi, \xi')$ , namely the diagonal part  $V(\xi, \xi)$  and the elements with the first energy corresponding to the Fermi level  $V(0, \xi')$ ; in the lower panel a graphical representation of the whole function in the TF and in RPA approximation is presented. The Sham–Kohn approach gives a smooth function, with no correlation with the electronic structure of the material. The upturn at about  $-18$  eV corresponds to the energy of the  $\mathbf{k} = 0$  state in a free-electron gas with the same number of electrons per unit cell. The use of TF approximation with the Bloch wavefunctions shows the effect of the orbital nature of states reflected in the matrix elements. In figure 3, for example, we see the strong Coulomb repulsion between very localized Ca d states giving a peak in the Coulomb matrix elements for  $\xi \simeq \xi' \simeq 4$  eV. The strong localization implies a nearly zero interaction between these states and the rest of the electronic structure (the darkest regions in the matrix), whose charge is located in different areas. Moreover, we can distinguish the signature of the  $sp^2$  bonds in the region  $-20$  to  $-5$  eV in a sharp increase of the matrix elements with poor interaction with higher energy states.

Going from Thomas–Fermi to diagonal-RPA screening does not introduce any important changes. Local field effects, on the other hand, strongly reduce the matrix elements below the Fermi level. In the high energy region all the approximations behave in a similar way as the states are free-electron-like. The RPA including local field effects, although giving similar structures with respect to the Bloch wavefunctions and TF approach, introduces a more efficient screening in the graphene layer so that the corresponding matrix elements are reduced by about 20%.

#### 4.3. Effects of anisotropy in the phonon coupling

It is interesting, at this point of the discussion, to analyze the role of the e-ph interaction anisotropy and its effects on  $T_c$  and on the anisotropic character of the superconducting gap.

**Figure 3.** Comparison between different approximations in calculating the Coulomb matrix elements (MEs). The central panel shows, with a scale of colors, the matrix of averaged Coulomb MEs (defined in equation (13)). Because this matrix is symmetric, we used the upper-left part to show Thomas–Fermi MEs (using Bloch wavefunctions) and the bottom-right part for RPA MEs. The upper panel shows two cuts of this matrix for the various approximations discussed in the text: a diagonal cut ( $V(\xi, \xi)$ , straight lines) and an horizontal cut passing for  $E_F$  ( $V(0, \xi')$ , dashed lines). On the right is the density of electronic states.

From a multiband BCS model (i.e. the Suhl–Matthias–Walker model [41]), it is known that an anisotropy in the phonon coupling always yields a  $T_c$  enhancement with respect to an averaged coupling. To discuss this kind of anisotropy, it is useful to compare  $\text{CaC}_6$  with  $\text{MgB}_2$ , the prototypical two-gap superconductor. We first define the band-resolved e-ph coupling  $\lambda_{ij} = \int \alpha^2 F_{ij}(\omega)/\omega d\omega$  and Eliashberg functions  $\alpha^2 F_{ij}$ :

$$\alpha^2 F_{ij}(\omega) = \frac{1}{N_i} \sum_{\mathbf{k}, \mathbf{k}'} \sum_{\nu} |g_{\mathbf{k}, \mathbf{k}', \nu}^{ij}|^2 \delta(\xi_{i\mathbf{k}}) \delta(\xi_{j\mathbf{k}'}) \delta(\omega - \omega_{\mathbf{q}\nu}), \quad (15)$$

where  $i$  and  $j$  are the indices of the selected sheet of the Fermi surface;  $N_j$  is the partial DOS at the Fermi level, for the sheet  $j$ ;  $|g_{\mathbf{k}, \mathbf{k}', \nu}^{ij}|^2$  are the e-ph matrix elements;  $\nu$  is the phonon branch; and  $\omega_{\mathbf{q}\nu}$  the phonon frequencies. Moreover, we define the DOS-renormalized, band-resolved matrix elements  $V_{ij}^{\text{ph}} = \lambda_{ij}/N_j$ .

In the following, we present the partial DOS and couplings for  $\text{CaC}_6$  and  $\text{MgB}_2$ : for  $\text{CaC}_6$  we separate the Fermi surface into three parts: (1) external  $\pi$  bands, (2) Ca sphere, and (3) internal  $\pi$  bands (the one cutting the Ca sphere, as shown in figure 1). We obtained

$$\lambda: \begin{bmatrix} 0.286 & 0.173 & 0.223 \\ 0.518 & 0.315 & 0.425 \\ 0.382 & 0.245 & 0.303 \end{bmatrix}$$



$$V^{\text{ph}} [\text{eV}]: \begin{bmatrix} 0.363 & 0.651 & 0.492 \\ 0.651 & 1.177 & 0.932 \\ 0.492 & 0.932 & 0.678 \end{bmatrix}$$

$$\text{DOS} \left[ \frac{\text{states}}{\text{eV} \cdot \text{cell}} \right]: \begin{bmatrix} 0.79 \\ 0.27 \\ 0.45 \end{bmatrix}.$$

For  $\text{MgB}_2$  we have [34]

$$\lambda: \begin{bmatrix} 1.017 & 0.213 \\ 0.156 & 0.448 \end{bmatrix}$$

$$V^{\text{ph}} [\text{eV}]: \begin{bmatrix} 3.390 & 0.520 \\ 0.520 & 1.093 \end{bmatrix}$$

$$\text{DOS} \left[ \frac{\text{states}}{\text{eV} \cdot \text{cell}} \right]: \begin{bmatrix} 0.30 \\ 0.41 \end{bmatrix}$$

where the first entry in each row or column corresponds to the two  $\sigma$  bands and the second to the  $\pi$  [42].

These data show clearly that both systems are quite anisotropic: in  $\text{MgB}_2$ , the much stronger coupling in the  $\sigma$  rather than in the  $\pi$  Fermi surfaces, and the small interband coupling, make the calculated anisotropic  $T_c$  double with respect to the isotropic one [6, 34]. Within the Suhl–Matthias–Walker model [41] this can be roughly explained by a large  $\lambda_{\text{max}} = 1.070$  (defined as the maximum eigenvalue of the  $\lambda_{ij}$  matrix—very similar to  $\lambda_{11}$ ) with respect to the average, isotropic coupling  $\bar{\lambda} = 0.860$ .

In  $\text{CaC}_6$ , instead, both Ca and C bands contribute strongly to the global coupling. Consider the Ca spherical Fermi surface, that in  $\text{CaC}_6$  has the largest superconducting gap. As shown by the  $\lambda_{ij}$  matrix, the contribution coming from the interband scattering is larger than the intraband one ( $\lambda_{21} = 0.518$  and  $\lambda_{23} = 0.425$ , against the intraband  $\lambda_{22} = 0.315$ ): although the Ca intraband average coupling (as represented by the  $V_{ij}^{\text{ph}}$  matrix) is the largest one, the large phase space (DOS) for interband scattering, with a reasonably large interband scattering potential, makes the difference. We calculated  $\lambda_{\text{max}} = 0.912$  and  $\bar{\lambda} = 0.855$ , both much larger than any of the intraband couplings. These arguments are supported by the SCDFT result: using the isotropic approximation we obtain a critical temperature of 8.1 K, against  $T_c = 9.4$  K obtained within the fully anisotropic approach. Hence, unlike in  $\text{MgB}_2$ , we have only a 15% reduction of  $T_c$  in comparison with the anisotropic case.

## 5. H under pressure

The possibility of a superconducting dense molecular phase of hydrogen represents a long-standing problem, recently investigated by means of first-principles methods within the SCDFT [14]. The low temperature and high pressure (>400 GPa) phase of molecular hydrogen is predicted to be a base-centered orthorhombic metallic molecular solid (known as the *Cmca* phase) [43] with two molecules per unit cell located on different layers. The electronic band structure arises from the bonding and anti-bonding combination of the  $\text{H}_2$  molecular orbitals. At high pressure, the band overlap between the valence and conduction bands produces a complex

Fermi surface with disconnected sheets of different orbital nature [14]. The molecular nature of the bands provides a strong electron–phonon coupling. The superconducting properties of this system are extremely interesting: the calculated  $T_c$  results in being around 240 K at  $\simeq 450$  GPa, with three different gaps on the three different sheets of the Fermi surface. The presence of three gaps represents one of the main peculiarities of molecular hydrogen, and its origin is mainly due to the (band) anisotropy of the electron–phonon coupling [14]. However, as we will see, the anisotropy of the Coulomb interaction is fundamental to achieve a proper prediction of the gaps at  $T = 0$  K.

In order to simplify the analysis, we will use a multigap BCS model (with parameters calculated *ab initio*) to discuss the effect of multiband anisotropy, with particular attention to the Coulomb interactions. Thus, we reduce the fully anisotropic SCDFT gap equation to a BCS multiband equation, including phonon renormalization effects (which, in the SCDFT gap equation (12) are included in the term  $Z_{n\mathbf{k}}$ ). In order to do this, we need the band-resolved interaction matrices, calculated averaging the  $\mathbf{k}$ -resolved e–ph and e–e matrix elements over (physically) different sheets of the Fermi surface.

In figure 4 we show the calculated Fermi surface at 414 GPa. The three gaps separate into three main regions: the disk at the Gamma point (labeled as 1), the ‘prism-like’ regions (2), and the remainder (unlabeled). In order to construct a three-band model of the system, we introduce a  $3 \times 3\lambda$ -matrix of the partial e–ph coupling  $\lambda_{ij}$ , where the indices  $i, j = 1, 2, 3$  span over the above mentioned regions. We also introduce the  $3 \times 3$  matrix for the  $V^{\text{ph}}$ , as defined in section 4.3. In analogy with the e–ph interaction, we also introduce the  $3 \times 3$  Coulomb interaction matrix  $V_{ij}^{\text{el}}$  and the  $\mu_{ij}$  matrix defined by the relation  $\mu_{ij} = N_j V_{ij}^{\text{el}}$ .  $V_{ij}^{\text{el}}$  represents the band-resolved Coulomb matrix defined in analogy with the definition of  $\lambda_{ij}$ , but containing the Coulomb matrix elements. In the following, we report the values of these matrices:

$$V^{\text{ph}} [\text{Ryd}]: \begin{bmatrix} 2.16 & 3.00 & 1.59 \\ 3.00 & 0.45 & 0.91 \\ 1.59 & 0.91 & 0.78 \end{bmatrix}$$

$$V^{\text{el}} [\text{Ryd}]: \begin{bmatrix} 0.71 & 0.08 & 0.11 \\ 0.08 & 0.38 & 0.20 \\ 0.11 & 0.20 & 0.20 \end{bmatrix}$$

$$\lambda: \begin{bmatrix} 0.14 & 0.37 & 1.45 \\ 0.20 & 0.06 & 0.82 \\ 0.11 & 0.11 & 0.71 \end{bmatrix}$$

$$\mu: \begin{bmatrix} 0.046 & 0.010 & 0.100 \\ 0.006 & 0.046 & 0.180 \\ 0.007 & 0.025 & 0.182 \end{bmatrix}.$$

We note that the intraband scattering ( $V_{ii}^{\text{el}}$ ) is dominating the Coulomb interaction and that it is particularly strong for the states of region (1). These states are bonding combinations of anti-bonding molecular states, are responsible for the interlayer bonding, and are very localized in the interlayer region, with rather poor screening properties. An opposite behavior characterizes the  $\mu$ -matrix, which represents the effective e–e interaction in the superconducting phase: in fact, despite



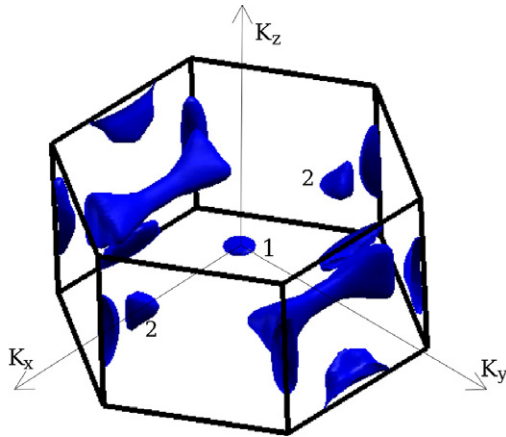


**Figure 4.** Fermi surface of molecular hydrogen at 414 GPa. The different sheets used to construct the interaction matrices are labeled as (1): the disk region; (2): the ‘prism-like’ regions; the remaining regions (not labeled).

the large value of  $V_{11}^{\text{el}}$  we find a very small value of  $\mu_{11}$ , due to the low density of states in region (1). Interband terms, in particular those involving the bands less coupled with phonons, dominate thanks to their high density of states. Although inspection of the  $\mu$ -matrix suggests a minor role of the e–e interaction anisotropy in the  $T_c$  value (we find the same  $T_c$  in the isotropic and anisotropic case), we demonstrate that inclusion of band anisotropy in the repulsive term has a nontrivial effect on the  $T = 0$  K gap. The phonon-renormalized BCS equation (RBCS) is obtained from the SCDFT fully anisotropic equation averaging the  $\mathbf{k}$ -anisotropy (still retaining the band anisotropy) and performing the  $T \rightarrow 0$ ,  $\xi, \xi' \rightarrow 0$  limits. The results of the solution of the RBCS equation are reported in table 2.

As we can see from table 1, the presence of three gaps is predicted even within the RBCS model. Comparing the results of the full RBCS and RBCS (e–ph) models, the role of both interaction on the prediction of  $T = 0$  gaps is evident. Even if the main source of band anisotropy is given by the e–ph interaction, inclusion of the proper band-resolved Coulomb interaction increases the anisotropy by about 18%.

This demonstrates that the band anisotropy of the repulsive e–e interaction, essentially related to the different nature of the bands at the Fermi level, increases the multigap superconducting properties in dense molecular hydrogen.

## 6. Summary

The SCDFT approach allows a fully anisotropic description of the superconducting phase and the inclusion of Coulomb repulsion effects on an *ab initio* basis. After a brief review of the SCDFT method, in this paper we performed a detailed analysis of the Coulomb and electron–phonon matrix elements in intercalated graphite  $\text{CaC}_6$  and hydrogen under high pressure. In  $\text{CaC}_6$  we studied different approximations for the Coulomb interaction. We find that, due to the presence of strongly localized states, the use of free-electron-like Coulomb matrix elements gives a strong underestimation of the Coulomb

repulsion and a corresponding overestimation of the critical temperature  $T_c$ . While local field effects are important to describe the screening properties in the graphene layers, the inclusion of an isotropic Coulomb interaction—averaged on isoenergy surfaces—does not strongly affect the value of  $T_c$ . Concerning the electron–phonon interaction, however, the isotropic approximation yields a  $T_c$  reduction of 15%.

Finally, we calculate the matrix elements of both interactions for H under high pressure. By making use of a multiband BCS model using SCDFT-calculated parameters, we demonstrate that the usual isotropic approximation of the repulsive e–e interaction is completely unjustified in the case of superconducting molecular hydrogen, and that the Coulomb anisotropy is fundamental for the prediction of the three superconducting gaps at  $T = 0$  K.

## Acknowledgments

This work makes use of results produced by the Cybersar Project managed by the Consorzio COSMOLAB, co-funded by the Italian Ministry of University and Research (MUR) within the Programma Operativo Nazionale 2000–2006 ‘Ricerca Scientifica, Sviluppo Tecnologico, Alta Formazione’ per le Regioni Italiane dell’Obiettivo 1 Asse II, Misura II.2 Società dell’Informazione. Work partially supported by the Italian Ministry of Education, through PRIN 200602174 project, by INFN-CNR through a supercomputing grant at Cineca (Bologna, Italy), by the Deutsche Forschungsgemeinschaft and by NANOQUANTA Network of Excellence.

## References

- [1] Eliashberg G M 1960 Interactions between electrons and lattice vibrations in a superconductor *Sov. Phys.—JETP* **11** 696
- [2] McMillan W L 1968 Transition temperature of strong-coupled superconductors *Phys. Rev.* **167** 331
- [3] Schrieffer J R, Scalapino D J and Wilkins J W 1963 Effective tunneling density of states in superconductors *Phys. Rev. Lett.* **15** 336
- [4] Lüders M, Marques M A L, Lathiotakis N N, Profeta G, Fast L, Continenza A, Massidda S and Gross E K U 2005 *Ab initio* theory of superconductivity—I: density functional formalism and approximate functionals *Phys. Rev. B* **72** 024545
- [5] Marques M A L, Lüders M, Lathiotakis N N, Profeta G, Floris A, Fast L, Continenza A, Gross E K U and Massidda S 2005 *Ab initio* theory of superconductivity—II: application to elemental metals *Phys. Rev. B* **72** 024546
- [6] Floris A *et al* 2005 Superconducting properties of  $\text{MgB}_2$  from first principles *Phys. Rev. Lett.* **94** 037004
- [7] Sanna A, Profeta G, Floris A, Marini A, Gross E K U and Massidda S 2007 Anisotropic gap of superconducting  $\text{CaC}_6$ : a first-principles density functional calculation *Phys. Rev. B* **75** 020511
- [8] Gonnelli R *et al* 2008 Evidence for gap anisotropy in  $\text{CaC}_6$  from directional point-contact spectroscopy *Phys. Rev. Lett.* **100** 207004
- [9] Nagel U, Hübner D, Joon E, Kim J S, Kremer R K and Room T 2008 Far-infrared signature of the superconducting gap in intercalated graphite  $\text{CaC}_6$  *Phys. Rev. B* **78** 041404(R)
- [10] Emery N *et al* 2005 Superconductivity of bulk  $\text{CaC}_6$  *Phys. Rev. Lett.* **95** 087003

- [11] Calandra M and Mauri F 2005 Theoretical explanation of superconductivity in  $C_6Ca$  *Phys. Rev. Lett.* **95** 237002
- [12] Kim J S, Kremer R K and Boeri L 2006 Specific heat of the Ca-intercalated graphite superconductor  $CaC_6$  *Phys. Rev. Lett.* **96** 217002
- [13] Ashcroft N W 1968 Metallic hydrogen: a high-temperature superconductor? *Phys. Rev. Lett.* **21** 1748
- [14] Cudazzo P *et al* 2008 High-temperature electron–phonon superconductivity in molecular hydrogen under extreme pressure *Phys. Rev. Lett.* **100** 257001
- [15] Narayana C *et al* 1998 *Nature* **393** 46  
Loubeyre P *et al* 2002 *Nature* **416** 613
- [16] Oliveira L N, Gross E K U and Kohn W 1988 Density functional theory for superconductors *Phys. Rev. Lett.* **70** 2430
- [17] Dreizler R M and Gross E K U 1990 *Density Functional Theory* (Berlin: Springer)
- [18] Hohenberg P and Kohn W 1964 Inhomogeneous electron gas *Phys. Rev.* **136** B864
- [19] Vonbarth U and Hedin L 1972 *J. Phys. C: Solid State Phys.* **5** 1629
- [20] Kreibich T and Gross E K U 2001 Multicomponent density-functional theory for electrons and nuclei *Phys. Rev. Lett.* **86** 2984
- [21] Kreibich T, van Leeuwen R and Gross E K U 2008 Multicomponent density-functional theory for electrons and nuclei *Phys. Rev. A* **78** 022501
- [22] Kurth S 1995 Exchange–correlation functionals for inhomogeneous superconductors *PhD Thesis* Julius-Maximilians-Universität Würzburg [http://www.physik.fu-berlin.de/~ag-gross/theses/kurth\\_phd.pdf](http://www.physik.fu-berlin.de/~ag-gross/theses/kurth_phd.pdf)
- [23] Lüders M 1998 Density functional theory for superconductors: a first principles approach to the superconducting phase *PhD Thesis* Julius-Maximilians-Universität Würzburg [http://www.physik.fu-berlin.de/~ag-gross/theses/lueders\\_phd.pdf](http://www.physik.fu-berlin.de/~ag-gross/theses/lueders_phd.pdf)
- [24] Marques M M 2000 Density functional theory for superconductors: exchange and correlation potentials for inhomogeneous systems *PhD Thesis* Julius-Maximilians-Universität Würzburg [http://www.physik.fu-berlin.de/~ag-gross/theses/marques\\_phd.pdf](http://www.physik.fu-berlin.de/~ag-gross/theses/marques_phd.pdf)
- [25] Bogoliubov N N, Tolmachov V V and Širkov D V 1958 A new method in the theory of superconductivity *Fortschr. Phys.* **6** 605
- [26] Gross E K U and Kurth S 1991 Density functional theory of the superconducting state *Int. J. Quantum Chem. Symp.* **25** 289
- [27] Lueders M, Marques M A L, Floris A, Profeta G, Lathiotakis N N, Franchini C, Sanna A, Continenza A, Massidda S and Gross E K U 2006 Density functional theory for superconductors *Psi-k Newsletter* 76 (Scientific highlight of the month)
- [28] Lueders M and Gross E K U 1995 Frequency-dependent linear response of superconducting systems *Int. J. Quantum Chem.* **56** 521
- [29] Wacker O-J, Kümmel R and Gross E K U 1994 Time-dependent density-functional theory for superconductors *Phys. Rev. Lett.* **77** 2915
- [30] Marini A SELF code <http://www.fisica.uniroma2.it/~self>
- [31] Floris A, Sanna A, Massidda S and Gross E K U 2007 Two-band superconductivity in Pb from *ab initio* calculations *Phys. Rev. B* **75** 054508
- [32] Profeta G, Franchini C, Lathiotakis N N, Floris A, Sanna A, Marques M A L, Lüders M, Massidda S, Gross E K U and Continenza A 2006 Superconductivity in lithium, potassium, and aluminum under extreme pressure: a first-principles study *Phys. Rev. Lett.* **96** 047003
- [33] Sanna A, Franchini C, Floris A, Profeta G, Lathiotakis N N, Lüders M, Marques M A L, Gross E K U, Continenza A and Massidda S 2006 *Ab initio* prediction of pressure-induced superconductivity in potassium *Phys. Rev. B* **73** 144512
- [34] Floris A *et al* 2007 Superconducting properties of  $MgB_2$  from first principles *Physica C* **456** 45
- [35] QUANTUM ESPRESSO code <http://www.quantum-espresso.org/>
- [36] Csányi G, Littlewood P B, Nevidomskyy A H, Pickard C J and Simons B D 2005 The role of interlayer state in the electronic structure of superconducting graphite intercalated compounds *Nat. Phys.* **1** 42
- [37] Mazin I I 2005 Intercalant-driven superconductivity in  $YbC_6$  and  $CaC_6$  *Phys. Rev. Lett.* **95** 227001
- [38] Calandra M and Mauri F 2006 Possibility of superconductivity in graphite intercalated with alkaline earths investigated with density functional theory *Phys. Rev. B* **74** 094507
- [39] Sham L J and Kohn W 1966 One-particle properties of an inhomogeneous interacting electron gas *Phys. Rev.* **145** 561
- [40] Posternak M, Baldereschi A, Freeman A J, Wimmer E and Weinert M 1983 Prediction of electronic interlayer states in graphite and reinterpretation of alkali bands in graphite intercalation compounds *Phys. Rev. Lett.* **50** 761
- [41] Suhl H, Matthias B T and Walker L R 1959 BCS theory of superconductivity in the case of overlapping bands *Phys. Rev. Lett.* **3** 552
- [42] Golubov A A *et al* 2002 Specific heat of  $MgB_2$  in a one- and a two-band model from first-principles calculations *J. Phys.: Condens. Matter* **14** 1353
- [43] Pickard C J and Needs R J 2007 *Nat. Phys.* **3** 473